

## The investigation of heating and compression of high-aspect ratio targets with 'Delfin-1'

By N. G. BASOV, A. E. DANILOV, M. P. KALASHNIKOV,  
B. V. KRUGLOV, Yu A. MIKHAILOV, A. V. RODE,  
G. V. SKLIZKOV AND S. I. FEDOTOV

Lebedev Physical Institute, Leninsky Prospekt 53 Moscow, USSR

(Received 1 October 1983)

Experimental results on the compression of shell targets with aspect ratio  $A = 150\text{--}250$  in the "Delfin-1" installation are reported. The absorbed laser energy was 0.3 to 0.5 kJ. The maximum compression was  $3.5 \times 10^3$ , the velocity of target compression at the final stage was  $2.6 \times 10^7$  cm/s, neutron yield was  $10^6$  to  $10^7$  D-D neutrons per laser shot. The appearance of plasma corona filamentation correlated with compression stability destruction.

### 1. Introduction

During the last few years, with large scale thermonuclear laser installations, (Andre *et al.* 1978; Basov *et al.* 1977; Kato *et al.* 1979; Speck 1978; Scoberne 1978; Bunkenberg *et al.* 1981) two main gasdynamic regimes of shell target compression: exploding pusher (Speck *et al.* 1979) and ablative acceleration (Basov *et al.* 1977), have been investigated. The major problem which arises in the case of the ablative regime is the achievement of stable adiabatic compression of high-aspect-ratio spherical targets. These targets are expected to give high shell implosion velocity and large volume compression. The theoretical estimates of the compression stability of high-aspect-ratio shell targets show (Afanasiev *et al.* 1982) that a high quality of target and good space-time uniformity of illumination are required. For instance, in the case of thermonuclear shell targets with an aspect ratio,  $A = R/\Delta R \approx 100$ , the amplitude of low frequency initial perturbations must be smaller than 1%. The main aim of the experiments described here is the investigation of the compression stability of high-aspect-ratio ( $A \geq 150$ ) shell targets at the level of absorbed energy,  $E_{\text{abs}} = 0.3\text{--}0.5$  kJ, the measurement of neutron yield from gas-filled targets and the investigation of filamentation and its influence on the shell compression stability.

### 2. Laser installation 'Delfin-1'

The laser installation 'Delfin-1' is designed for experiments on heating and compression of shell targets in the ablative regime for a level of absorbed energy  $\sim 1$  kJ. A block-scheme of the installation is shown in figure 1. The installation is based on a Nd-glass laser with an energy output up to 3–5 kJ and a pulse duration 0.5–5 ns. The principle of successive-parallel amplification is used. At the output of the laser the 108 beams are each formed with an aperture  $\sim 40$  mm. Beam splitting is done with one-dimensional cylindrical collimators. The scheme of laser beam splitting is the following, figure 2, 1–2–6–12–36–108. Output amplifiers are constructed as 6-blocks, each one containing 18 active elements. Each 3 blocks form a power module as described in early work (Basov *et al.* 1978, Basov *et al.* 1981). The six light beams formed at the

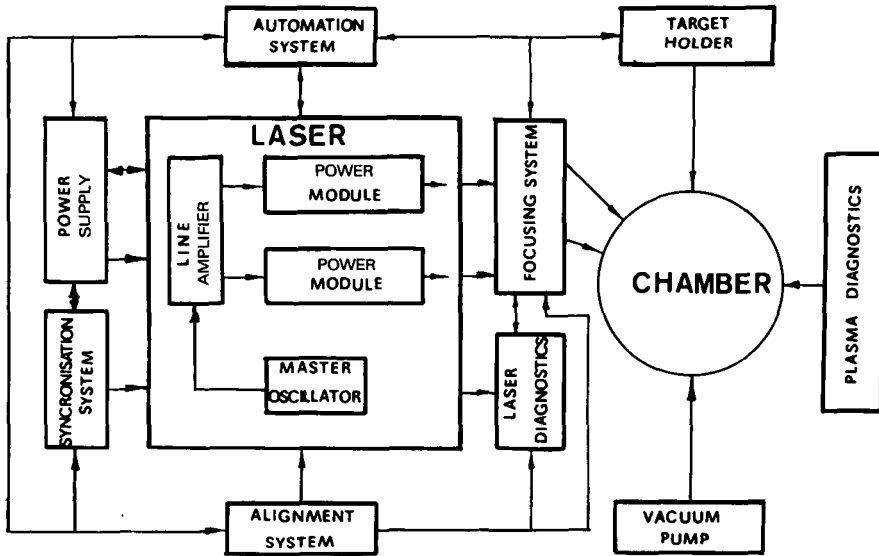


FIGURE 1. Block-scheme of laser installation 'Delfin-1'.

laser output are directed in the focusing system. Each channel of the focusing system consists of the following elements (figure 3): a mirror which joins 18 elementary beams into one composite beam with an aperture of 280 mm, the first lens of the focusing system which is used to adjust the aperture of the composite beam to the aperture of the aspherical lens, a turning mirror for fine alignment of focal spot position at the target surface, a correction element optical plate for laser beam diagnostics, an aspheric lens with precise mounting which makes it possible to align the focal spot position at the target in the direction of laser beam propagation with an accuracy of 15  $\mu\text{m}$ . The surfaces of all optical elements have antireflection coatings and the transmission of the

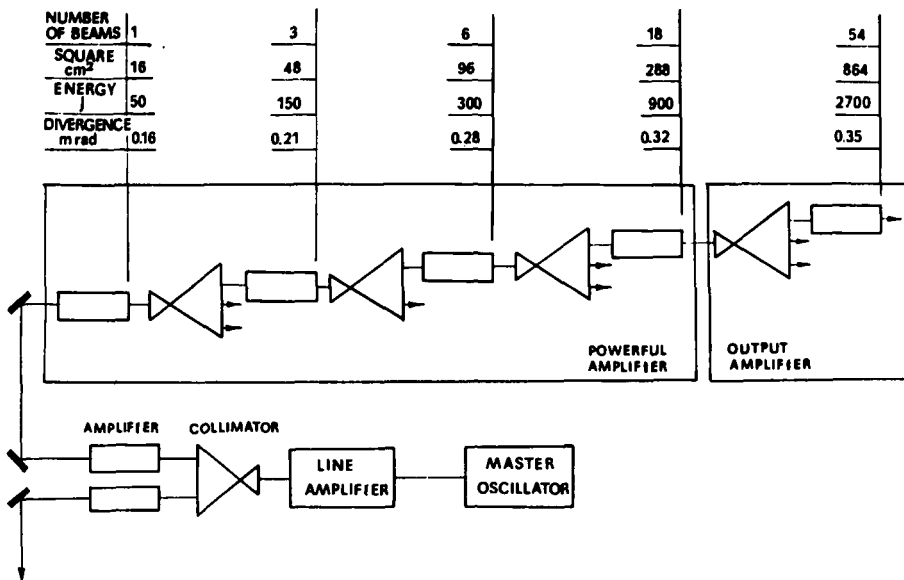


FIGURE 2. Scheme of laser beam splitting in power amplifiers.

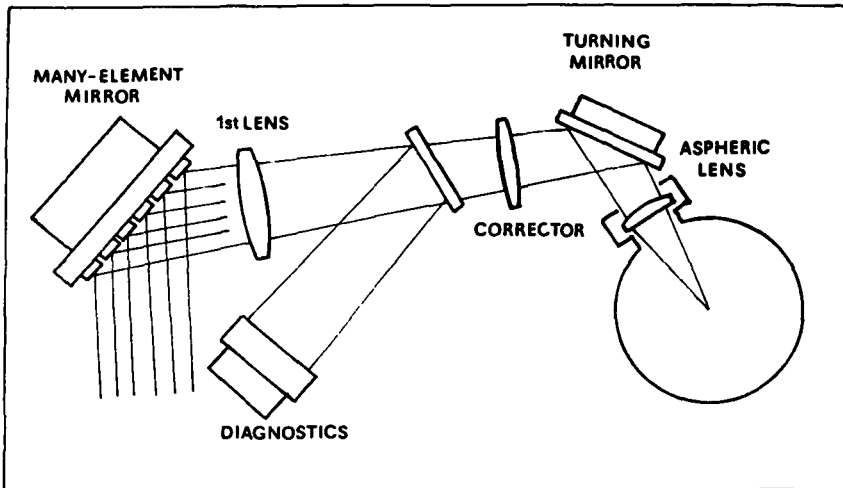


FIGURE 3. Scheme of a focusing channel.

focusing system is 85%. The effective focal length of the focusing system is 780 mm with an aperture  $d/f = 1/2 \cdot 4$ . The focal spot diameter of each composed beam has a dimension at the target plane of  $200 \mu\text{m}$ . For this reason shell targets with diameters  $200 \mu\text{m}$  and more may be used, at levels of flux density ( $10^{13}$  to  $10^{14}$ )  $\text{W}/\text{cm}^2$ .

The target chamber, figure 4, is a sphere of 560 mm in diameter with windows for laser beams and plasma diagnostics. The geometry of irradiation is cubical with an angle of deviation of the laser beam optical axis to the normal of the cubic planes  $\sim 16^\circ$ .

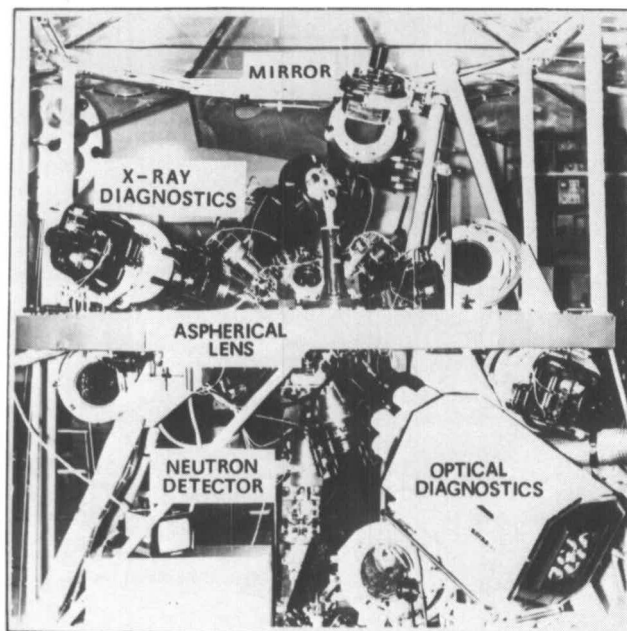


FIGURE 4. General view of target chamber.

### 3. Study of the laser radiation parameters

The most important parameters of the laser radiation from the view-point of thermonuclear fusion are the following: energy, spectral composition, brightness, contrast, polarization and degree of coherence.

The laser diagnostic complex includes (figure 5): calorimetric detectors measuring the laser and plasma parameters, devices and apparatus for the registration of fine structure of the radiation in the near and far fields, degree of coherence, spectral composition, contrast, polarization, etc. Along with the above the caustic structure of the composed beams in the target plane has been studied.

The output laser energy was about 250–350 J per composite beam and the total energy of the system 1.5–2 kJ. The energy of the radiation directed onto the target surface was 700 J; about 50% of the output energy.

The study of the angular structure of the radiation was made as described by Valuev *et al.* (1978). The total divergence at the output of the system of the composite beams was  $3.5 \times 10^{-4}$  rad. The measurements of the energy contained in the 'wings' of the intensity distribution in the far field have shown that no more than 20% of the energy was spread out of the main cone.

The brightness of the radiation at the laser output was  $B = 0.5 \times 10^{16}$  W/cm<sup>2</sup> ster., and this made it possible to reach the flux density  $q \approx (0.5 \text{ to } 1) \times 10^{14}$  W/cm<sup>2</sup> at the surface of a 500  $\mu$ m target using an f 2.4 lens in each of six focusing channels. The laser radiation contrast was measured using the method described in Danilov *et al.* (1978) and found to be  $K > 10^6$ , in the composite beam.

The results of numerical calculations using the six-beam scheme of the Delfin-1 focusing system have given evidence that the independent adjustment of the angle of

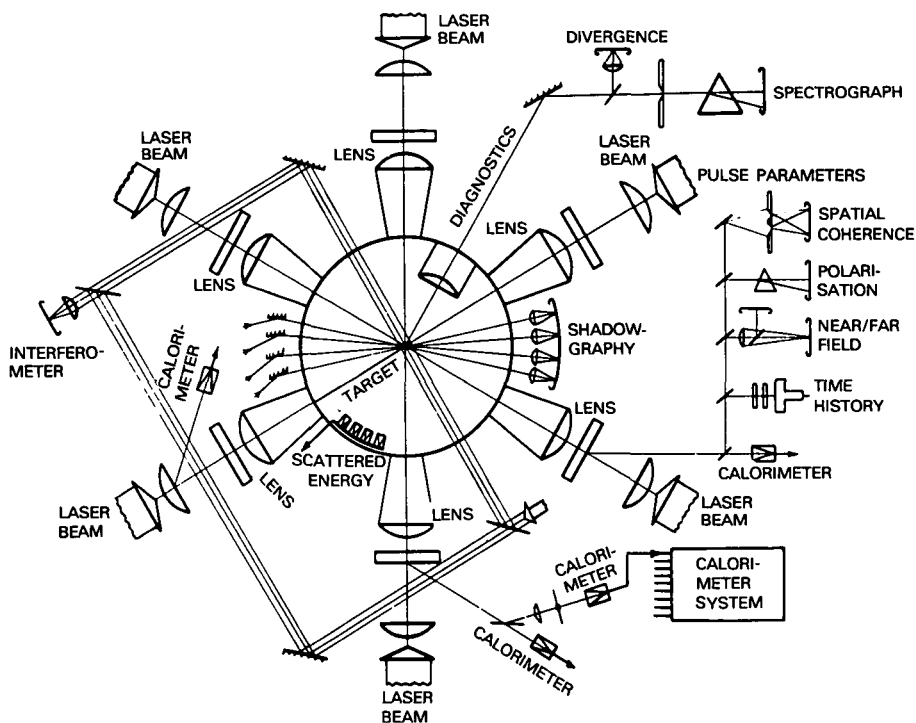


FIGURE 5. Laser diagnostics system.

orientation of each beam makes it possible to vary the level of target illumination within a few percent (7 to 10%) and to keep the energy losses negligibly small (Danilov *et al.* 1977). However, these calculations did not take into account the interference patterns which resulted in local extrema of illumination. The typical size of an interference speckle is determined by the radiation spatial coherence, and its amplitude depends on the monochromaticity and polarization of the interfering beams. The smallest size of the speckle is limited by the aberration of the focusing lens which was from 10 to 20  $\mu\text{m}$ . To measure the degree of coherence of the real laser beam at a flux density of more than 1  $\text{GW}/\text{cm}^2$ , a Fresnel biprism (figure 6) was used. Figure 7 shows a typical interferometric figure of the laser radiation at the output of the amplifying linear system. The degree of coherence determined from this interferogram does not exceed 0.15.

The value of spatial coherence at the laser output was about 20 mm, which resulted in the formation of the interferometric spikes at the target surface with a dimension between 20 and 50  $\mu\text{m}$ .

The polarization study has given evidence that only 20% of the output energy was linearly polarized when the input radiation was linear polarized with a polarization factor of  $10^5$ .

Spectral structure of the laser radiation has been studied at the output of the master-oscillator, at the preliminary amplification cascades and at the output of the

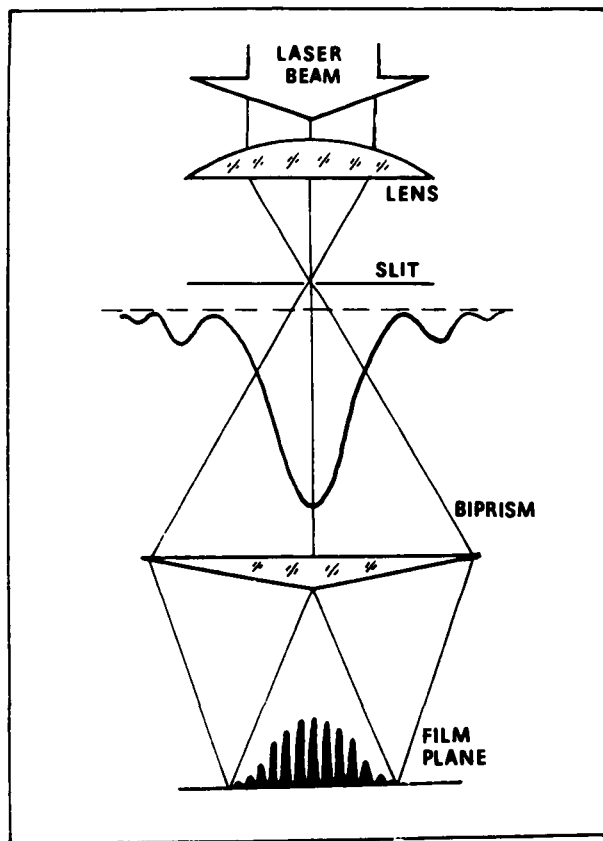


FIGURE 6. Scheme of interferometer for measurement of laser radiation coherence.

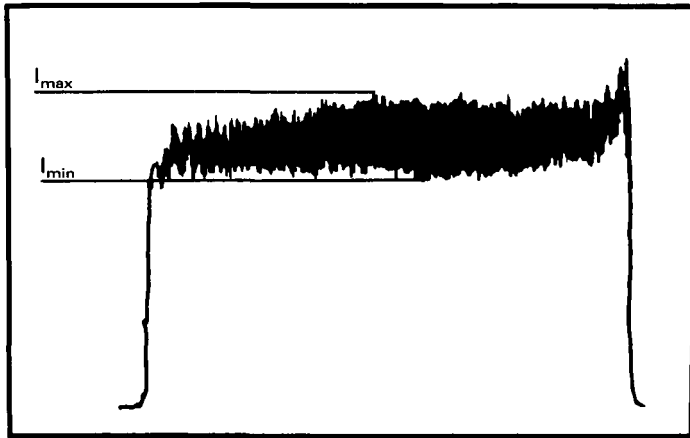


FIGURE 7. Interferogram of laser radiation from the linear-amplifier. Degree of coherence

$$\text{is } \gamma = \frac{I_{\max} - I_{\min}}{I_{\max} + I_{\min}} = 0.15.$$

laser power cascades. The results of measuring the radiation spectrum at the laser output are presented in figure 8. The effective spectral resolution is  $1.5 \text{ \AA}$ . It can be seen that the spectral halfheight band width is  $140 \text{ \AA}$ , and corresponds to a coherence length,  $L_{\text{coh}} \approx \lambda^2/\delta\lambda = 8 \times 10^{-3} \text{ cm}$ .

Low coherence and a high level of depolarization of the radiation in the full energy pulse determined the low amplitude of the intensity spikes in the caustic, 1 to 5%, (figure 9).

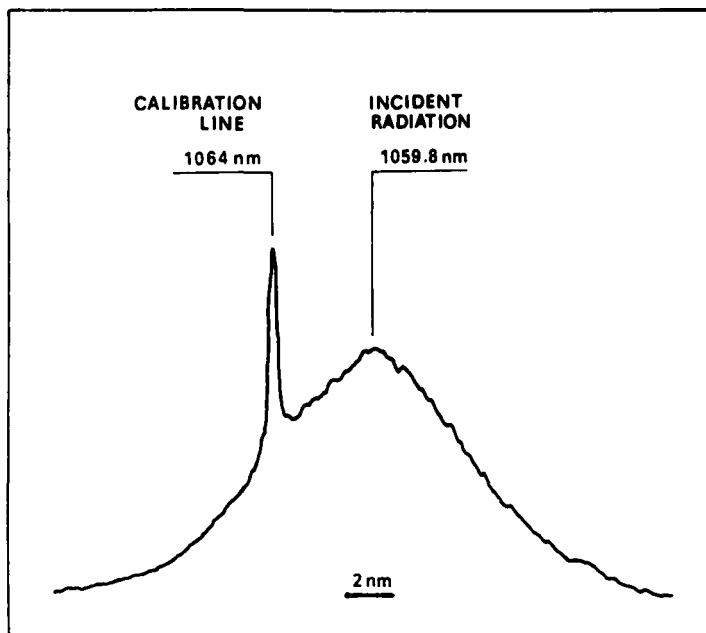


FIGURE 8. Spectra of laser radiation incident on the target.

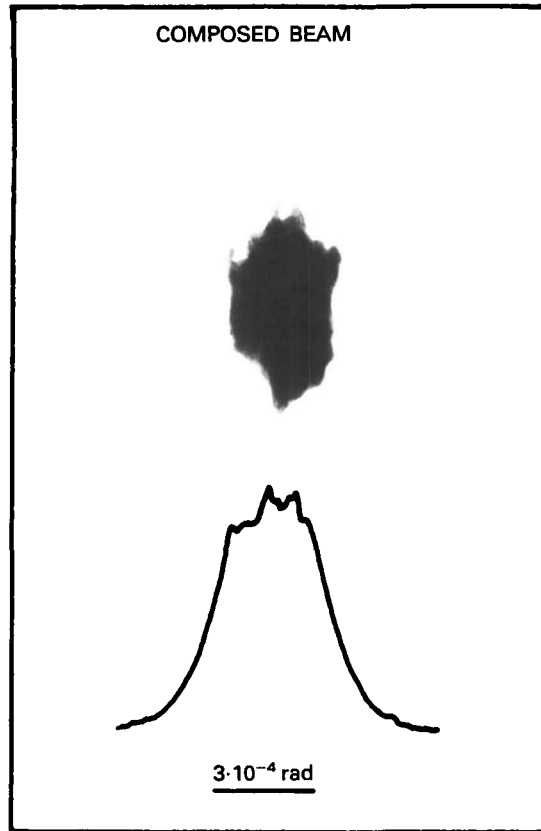


FIGURE 9. Angular distribution of composite beam radiation. Photograph of composite beam angular intensity distribution in far field. Angle containing 80% laser energy is  $2\alpha = 3.5 \times 10^{-4}$  rad.

#### 4. Study of laser radiation coupling in high aspect-ratio shell targets

One of the experimental problems to be solved was the question of the efficiency of the laser radiation energy deposited in the corona. To study the energy balance of the laser radiation directed onto the target surface the multichannel calorimetric system was used. This system enabled the energy of the radiation incident on the target to be defined, in addition to the energy passing through and reflected into the solid angle of the focusing lens, and the energy of the scattered and refracted radiation.

For spherical heating of the targets the energy balance can be written,  $E_1 = E_r + E_p + E_{sc} + E_{abs}$ , where  $E_1$  is the energy of the laser radiation incident onto the target,  $E_r$  is the energy of self-radiation in the visible and IR region ( $\lambda \geq 0.3 \mu\text{m}$ ) and the reflected laser energy into the aperture of the focusing optics,  $E_p$ , is the energy which passes through and around the target ( $\lambda \geq 0.3 \mu\text{m}$ ),  $E_{sc}$ , is the energy scattered by the plasma ( $\lambda \geq 0.3 \mu\text{m}$ , except  $E_r$  and  $E_p$ ) and  $E_{abs}$ , is the energy absorbed by the plasma.

The measurements of the values of  $E_r$  and  $E_p$  in the experiments on spherical heating of the targets with the 'Delfin-1' installation result in a total value of not more than 10 to 20% of  $E_1$ , and the relation between them depends on the material and the design of the target.

Figures 10 to 12 present the measured data on the scattered and absorbed laser

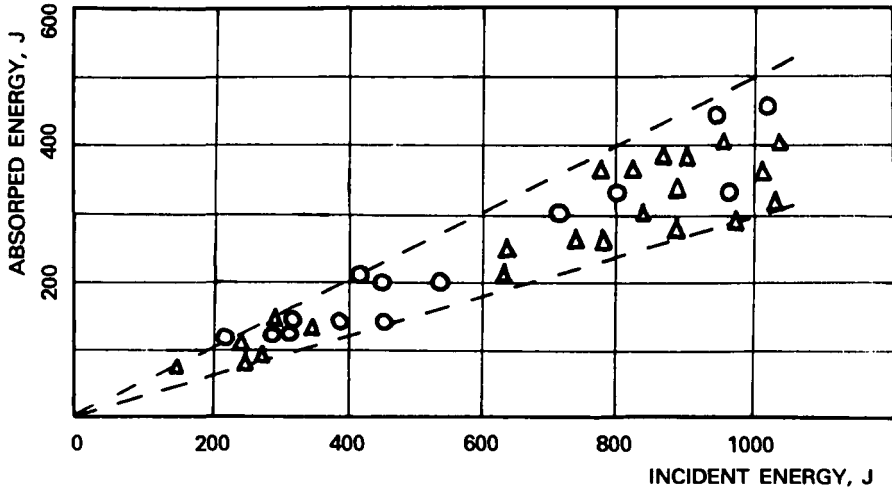


FIGURE 10. Absorbed energy versus incident energy.  $\circ$ , polysterene target,  $\Delta$ , glass target.

radiation. Figure 10 shows the dependence of  $E_{abs}$  on  $E_1$ . It is seen that the averaged fraction of the absorbed energy is 40–45% of  $E_1$ . The fraction of the absorbed energy remains unchanged with the variation of the flux density at the target surface, and it has a weak dependence on the target material.

Figure 11 illustrates the efficiency of the energy absorption as a function of the target size. The fraction of the absorbed energy increased from 35% up to 45% with an increase of the shell target diameter from 200 to 500  $\mu\text{m}$ . The more rapid increase of absorption is observed for polystyrene targets and the weaker dependence for glass ones. There is no increase of the absorption when the target diameter becomes more than 500  $\mu\text{m}$ .

Figure 12 demonstrates the dependence of the laser radiation energy, scattered in the chamber, on the target diameter and material. The data implies that the scattered energy fraction is slightly diminished with the increase of the target diameter from 300 up to 500  $\mu\text{m}$ . For high aspect ratio targets ( $A \geq 100$ ) it becomes 35%.

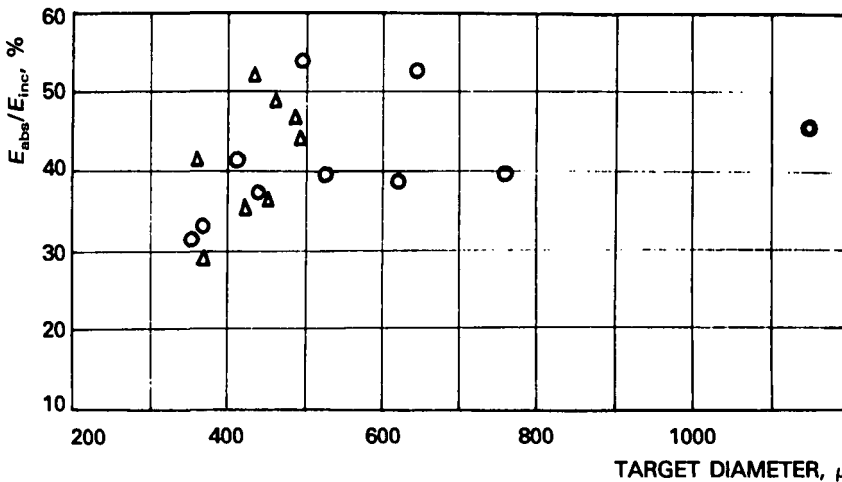


FIGURE 11. Absorption of laser radiation as a function of shell target diameter.  $\circ$ , polysterene target;  $\Delta$ , glass target.

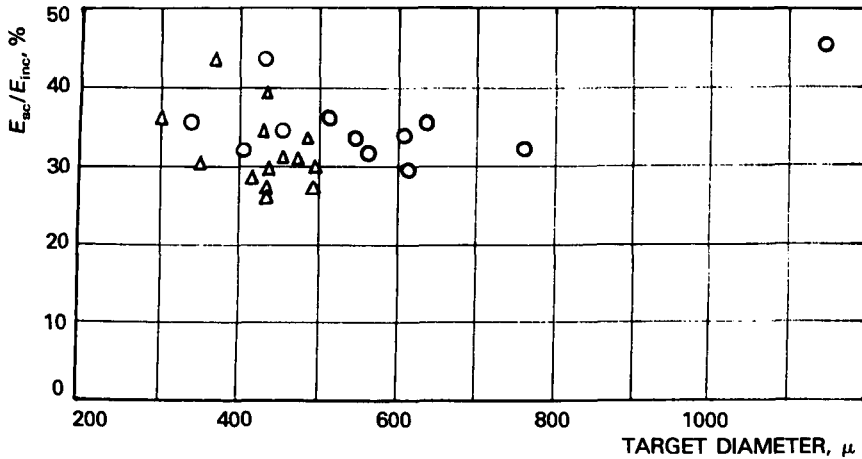


FIGURE 12. Dependence of scattered laser radiation upon diameter of the target. O, polysterene target; Δ, glass target.

In the experiments a laser light absorption value of 40 to 45% was observed for high aspect ratio targets. This value slightly exceeds the one obtained by Afanasiev *et al.* (1979a) and by Ripin *et al.* (1979) and is in good agreement with the calculations of Afanasiev *et al.* (1979b). The latter predict an increase of absorption coefficient with an increase of laser energy and target size for a fixed radiation flux density at the target surface and a fixed plasma temperature.

Another method used to measure the absorbed energy was multiframe laser high-speed shadow photography of the shock wave (SW), formed in a rarefied gas by the expansion of the hot dense plasma (Basov *et al.* 1967). In figure 13 a typical 19-frame

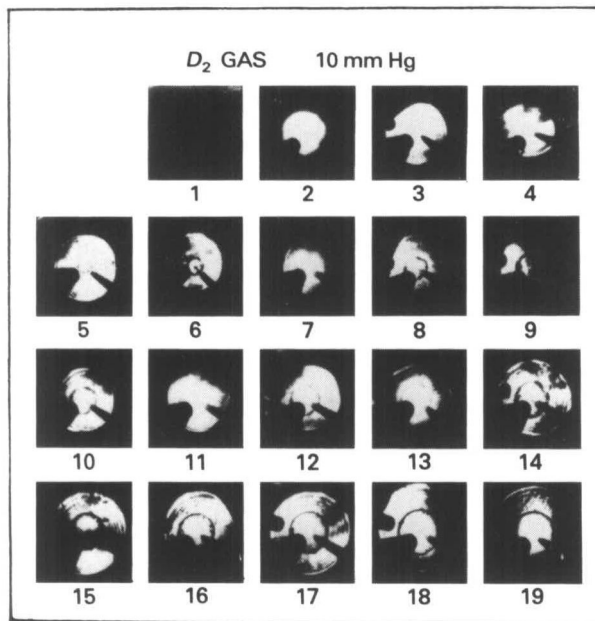


FIGURE 13. 19-frame schlieren-photograph of a strong shock wave formed by exploding target in residual gas. A relay laser is used as a light source for shock wave registration. Exposure time is 1 ns. Time intervals between frames are: (1-2) to (10-11) frames  $\Delta t = 6.6$  ns, (11-12) to (18-19) frames  $\Delta t = 125.4$  ns. Heating laser pulse arrives between frames 3 and 4.

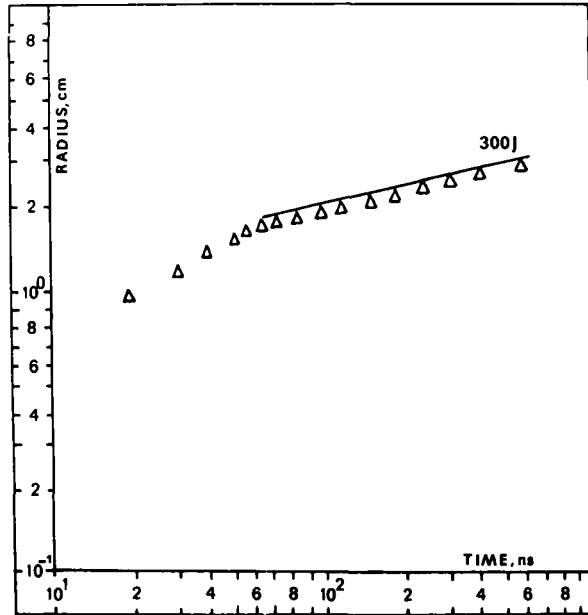


FIGURE 14. *R-t* diagram of shock wave in atmosphere of  $D_2$  gas at a pressure of 10 Torr. Solid line is solution of Sedov's model of shock wave expansion in the case of absorbed laser energy  $\sim 300$  J.

SW shadowgram generated by the plasma expanding in the residual gas atmosphere is shown. Figure 14 presents an *R-t* diagram of the SW motion. It is seen that the *R-t* diagram may be divided into two parts. A time proportional change of SW front radius is observed in the initial stages of expansion. The motion velocity is high and lies within the range  $(1.5-5) \times 10^7$  cm/s. This data allows the assumption that, at an initial stage of the SW, a 'snow plow' situation is realized. The front motion may be expressed (Basov et al. 1974) as,

$$R(t) = \frac{2}{\gamma - 1} \left( \frac{\gamma + 1}{2} \right)^{\frac{1}{2}} \left( \gamma \frac{R}{M} T_i \right)^{\frac{1}{2}} t,$$

where  $\gamma$  is the adiabatic index,  $R$  is the universal gas constant,  $M$  is the effective target atomic weight,  $T_i$  is the temperature of the expanding ions at the final moment of heating. The ion temperature value obtained by analysing the initial part of the *R-t* diagram is 900 eV, a value in agreement with the results obtained by X-ray methods.

By studying Sedov's spherical SW model (Sedov 1946) a lower bound of explosion power due to absorbed laser energy can be estimated. An SW having an energy of 200 to 300 J has been measured experimentally and this corresponds to an approximately 30% coefficient of absorption of laser energy in the plasma.

### 5. Study of high aspect shell target compression

Glass shells of diameter  $2R = 350$  to  $600 \mu\text{m}$  and aspect ratio  $R/\Delta R \approx 150$  to  $250$  were used in the experiments. Variations of shell thickness did not exceed 5%, and the nonsphericity of the target was  $\leq 0.5\%$ .

Registration and measurement of target volume compression were made by means of multi-channel pinhole cameras located in three mutually perpendicular directions forming the X-ray plasma image within the energy range  $E = 2$  to  $3$  keV and with

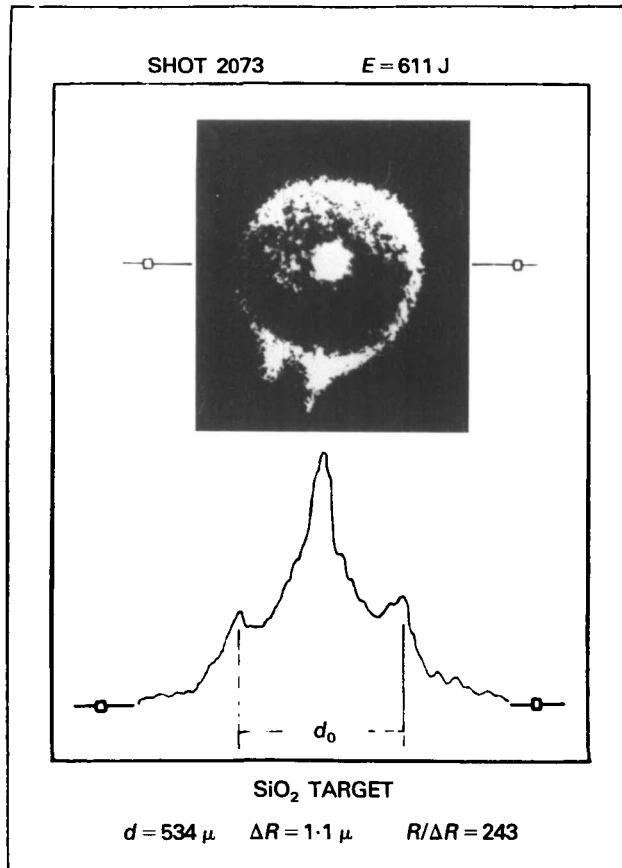


FIGURE 15. Microphotograph and densograph of high aspect ratio imploding glass target.

spatial resolution 10 to 20  $\mu\text{m}$ . Investigations of shell motion dynamics were made using an X-ray image-converter tube (operating as a streak camera) with temporal resolution  $\delta t = 1.3 \times 10^{-10}$  s and spatial resolution  $\delta r \approx 50 \mu\text{m}$ .

Figure 15 shows a pin-hole photograph and its microdensograph obtained from a glass target of 534  $\mu\text{m}$  diameter and  $A = 234$  aspect ratio with energy incident on the target of  $E_1 = 611$  J; the absorbed energy,  $E_{\text{abs}}$ , was 250 J. The volume compression value,  $V_0/V = 3.4 \times 10^2$ .

In figure 16 the space-time structure of the X-ray plasma radiation is presented for experiment 2128 obtained using an X-ray camera (Basov *et al.* 1982). The same figure shows the temporal shape of the laser pulse incident on the target. As can be seen from the figure, the time of the target motion towards the centre is 1.6 ns, and 60% of the incident energy is contained in this time interval. The measured value of the mean velocity of shell motion towards the centre is  $\bar{C} \approx 160$  km/s, in agreement with estimates of mean compression velocity for targets of aspect ratio  $A \approx 200$  and a radiation flux density,  $q = 10^{14}$  W/cm<sup>2</sup> (Afanasiev 1980). Maximum compression velocity measured for the final stage is 260 km/s.

Table 1 presents the experimental data for glass shell compression which illustrates the effect of inhomogeneity on the compression. Target irradiation inhomogeneity was introduced by the distribution of the composite beam radiation over the microsphere

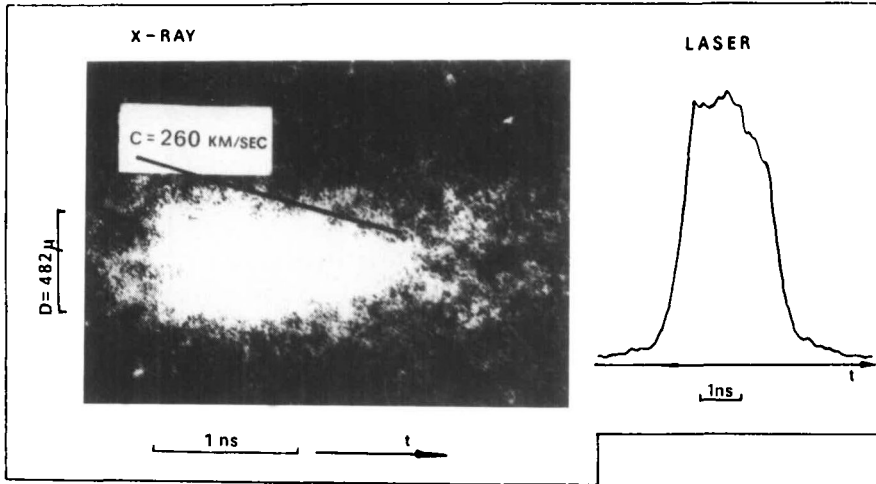


FIGURE 16. Time and space structure of X-rays for an imploding glass high aspect ratio target, obtained with the help of an X-ray streak camera. Spatial resolution of the streak camera is  $\sim 50 \mu\text{m}$ , time resolution is  $\sim 150 \text{ ps}$ . Solid line coincides with the speed of compression,  $C = 2.6 \times 10^7 \text{ cm/s}$ . Maximum speed of compression  $2.6 \times 10^7 \text{ cm/s}$  is achieved in the moment close to the maximum compression. Mean value of speed is  $\langle C \rangle = 1.6 \times 10^7 \text{ cm/s}$ .

surface (not exceeding 20% and changing slightly from shot to shot) and by the difference of energy in each composite beam.

Maximum volume compression  $V_0/V = 3.4 \times 10^3$  was obtained for a typical energy difference, in the composite beam, of  $\sim 9.8\%$ .

Figure 17 illustrates the effects of target symmetry and irradiation homogeneity on compression. The figure shows pinhole pictures, obtained from three mutually-perpendicular directions in experiment 2092. In this experiment the target was suspended from a  $40 \mu\text{m}$  diameter fiber. It can be seen that the compressed core is stretched in the direction of the fiber leg. The compression value is,  $V_0/V = 2.4 \times 10^3$ .

The attainment of such high compression values ( $\sim 3 \times 10^3$ ) for targets with an aspect ratio of  $A \approx 150$  to 250 may be conditioned by symmetrization of the target heating due to the electron heat conductivity caused by high plasma temperature in the corona,  $T_e \approx 1 \text{ keV}$ . Measurements of plasma electron temperature in the compressed core give a value of up to 2 keV.

Shot No.	Target diameter $\mu\text{m}$	Aspect ratio	Incident energy J	Inhomogeneity of irradiation, %	Volume compression
2073	534	243	611	20	$3.4 \times 10^2$
2075	579	207	634	13	$1.7 \times 10^3$
2092	534	224	979	7.5	$2.4 \times 10^3$
2093	541	225	1068	9.8	$3.5 \times 10^3$
2097	578	206	1078	15	$1.4 \times 10^3$
2098	543	199	855	25	$7.8 \times 10^2$
2101	382	147	926	15	$10^3$

TABLE 1

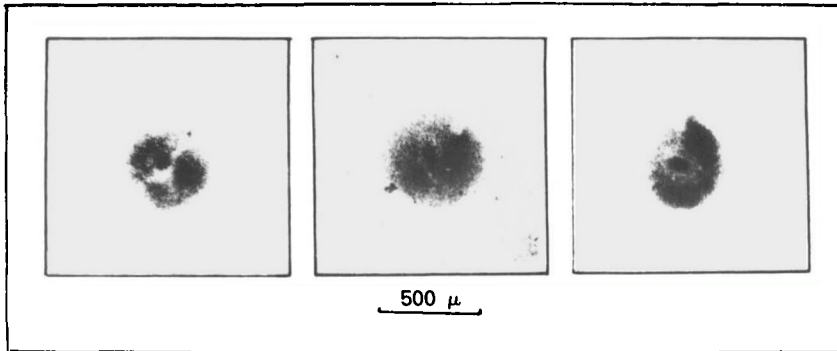


FIGURE 17. Pinhole photographs of imploding target from three perpendicular directions. The figure illustrates influence of target holder on the form of compressed region, which expands in the direction of the target holder. Volume compression evaluated from 3-dimensional image of compressed region is  $V_0/V = 2.4 \times 10^{-3}$ .

**6. Generation of D-D neutrons by compression of high aspect ratio targets**

In the majority of the preceding neutron experiments see, for example, Basov *et al.* (1977) in the regime of “hydrodynamic compression”, shells with a moderate aspect ratio ( $A \approx 30$  to  $50$ ) were used. The laser energy did not exceed 100 to 200 J which explains the low heating of the compressed core of the target ( $\sim 0.1$  to  $0.5$  keV) and the instability of the neutron yield, even when a considerable compression was achieved ( $\sim 10^3$ ). Deuterium filled (pressure,  $p = 3.8$  atm) glass shells of diameter  $2R = 200$  to  $500 \mu\text{m}$  were used in these contemporaneous experiments.

The diagnostics of the thermonuclear reactions during the heating and compression of the targets was done using three time-of-flight scintillator detectors (Nikolaev *et al.* 1980; Kirillov-Ugrumov *et al.* 1981) placed around the chamber at distances from 0.8 m to 3 m. Also two neutron monitors (Kirillov-Ugrumov *et al.* 1981) and a Kodak LP-115 detector, based on cellulose nitrate. The time of flight spectrometers and neutron monitors, with registration thresholds between  $4 \times 10^3$  and  $2 \times 10^6$  neutrons per shot made it possible to measure the absolute number of D-D-neutrons, generated in each experiment and the detector based on cellulose nitrate registered  $\text{He}^3$  and T nuclei. An electrical triggering pulse, the laser signal from the target plane, and an X-ray target radiation pulse were all used in the neutron detectors as origin points.

The use of the above variety of diagnostic methods has made it possible to fix the neutron yield reliably within the range of  $10^6$  to  $10^7$  D-D-neutrons per shot, in addition to the corresponding yield of  $\text{He}^3$  and T nuclei. Typical target and laser parameters of some Delfin-1 shots, when thermonuclear reactions were observed are shown in the table 2.

Experiment No.	Target, diameter $\mu\text{m}$	Aspect ratio	Energy at the target J	Inhomogeneity of irradiation	Volume compression
2127	469	247	543	38	$3 \cdot 10^2$
2128	482	193	785	19	$8 \cdot 10^2$
2130	439	159	781	23	$7 \cdot 10^2$
2131	411	147	683	27	$5 \cdot 10^2$

TABLE 2

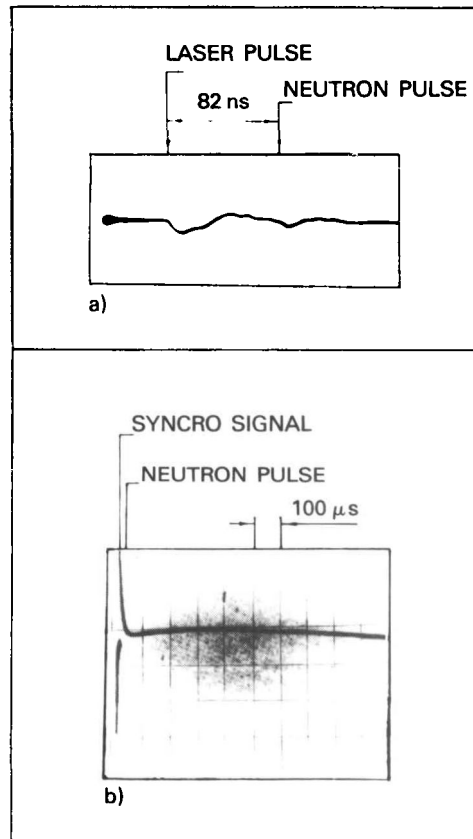


FIGURE 18. Oscillograms of neutron pulses at the level of neutron yield  $2 \times 10^6$  D-D neutrons per laser shot. (a) scintillator detector, (b) wide energy spectrum neutron monitor.

It should be noted that the large neutron yields were observed only in those experiments with a volume compression greater than  $10^2$  and a core temperature greater than 1 keV.

Typical oscillograms from the time-of-flight detector (a) and from the wide-bandwidth neutron monitor (b) are shown on figure 18. One positive monitor impulse is equivalent to a neutron yield of  $2 \times 10^6$ . The decrease of volume compression in neutron experiments, compared with the compression value of empty shells, can be explained by an inferior illumination symmetry, table 2, and also by the influence of thermonuclear fuel pressure on the process of shell implosion.

## 7. Observation of plasma corona filamentation

In a number of articles, devoted to thin shell compression plasma corona filamentation has been reported (Mochizuki *et al.* 1980; Herbst *et al.* 1981a; Will *et al.* 1982; Herbst *et al.* 1981b). The interest in filamentation phenomena is due to the following. In the hydrodynamic compression regime a high symmetry of ablation is necessary to achieve high fuel compression. In this case the presence of filamentation shows that their development in plasma can disturb the symmetry of shell compression.

Investigation of X-ray laser plasma radiation was carried out with three seven-frame pinholes, with different filters (*K*-edge 2.2 to 6.2 keV) positioned orthogonally. Pinhole

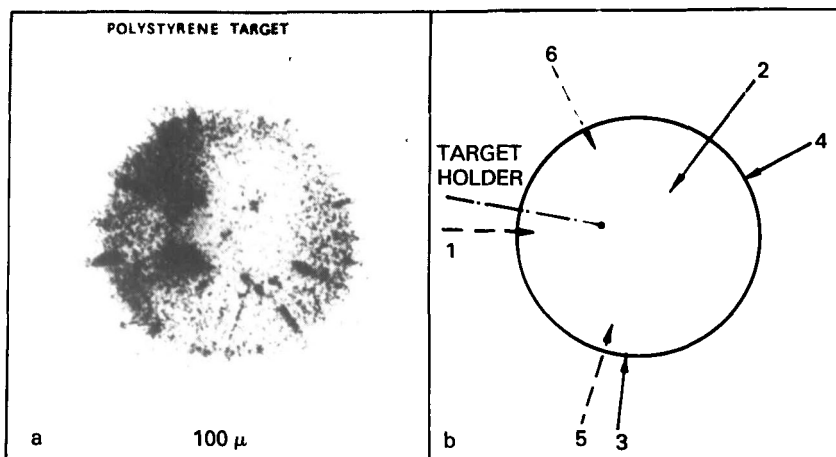


FIGURE 19. Filamentation of plasma corona (polystyrene target,  $2R = 580 \mu\text{m}$ ). Energy absorbed in the target,  $E_{\text{abs}} \approx 300 \text{ J}$ . (a) X-ray pinhole photograph of the target, (b) geometry of irradiation. The picture illustrates absence of correlation between beams and filament orientation.

resolution was from  $10$  to  $40 \mu\text{m}$  depending on pinhole size and magnification. Different shell materials (glass, polystyrene) and shell sizes (radius,  $R = 200$  to  $250 \mu\text{m}$ , aspect ratio  $R/\Delta R \approx 30$  to  $250$ ) were used in the experiments.

Plasma corona filamentation was observed with polystyrene shells. The X-Ray photograph (figure 19a) illustrates plasma when filamentation develops. This photograph was obtained in the experiment with a polystyrene shell of diameter,  $2R = 580 \mu\text{m}$ , an aspect ratio,  $R/\Delta R \approx 50$ , laser energy,  $E_{\text{las}} = 800$  and absorbed energy,  $E_{\text{ab}} = 380$ . Typical filament diameter near the target surface was about  $20$ – $40 \mu\text{m}$ . The total length of filaments was from  $100$  to  $200 \mu\text{m}$  and the greater the distance, the less the diameter. Figure 19b shows the laser beam geometry on the target surface. Comparison of (a) and (b) shows the absence of correlation between filaments and laser beam displacement.

The laser radiation and target variation show certain regularities in filamentation phenomena. The greater the target diameter, the greater the quantity and number of filaments on the target surface. Filamentation was observed in almost all experiments with polystyrene targets, when no compression was observed.

There was no corona filamentation in the experiments with glass shells, for laser pulse energies,  $E_{\text{las}} \approx 1 \text{ kJ}$ , and durations of  $2.3 \text{ ns}$  (flux density  $q = 10^{13}$ – $10^{14} \text{ V/cm}^2$ ). There was high volume compression ( $\sim 10^3$ ) in these experiments, figure 15. When filamentation appeared in some shots, figure 20, with glass shells, a compressed core was not observed.

The presence of filamentation, observed from emitted X-rays indicates the jet character of plasma expansion. The absence of a compressed core implies that the process of shell acceleration becomes unstable and volume compression sharply decreases. Such plasma expansion character can be attributed to cumulative phenomena in the corona, that develop when the plasma density distribution becomes nonspherical near the evaporating boundary. The source of the density perturbations may be initially small coherent ripples in the incident radiation that are amplified in the low density plasma corona by mechanisms of self-focusing. To change the distribution of laser intensity in the dense plasma it is necessary to satisfy,  $B > 2\pi$  (Basov *et al.* 1982). For

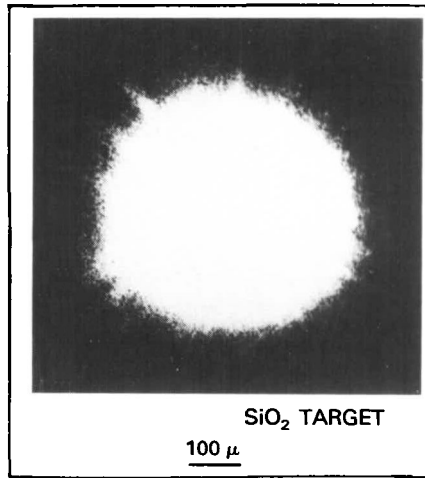


FIGURE 20. Filamentation of plasma corona in the case of a glass target. Target parameters:  $2R = 490 \mu\text{m}$ ,  $A = 240$ . Energy on the target  $E_{\text{inc}} = 1.2 \text{ kJ}$ .

spherical plasma the  $B$ -integral is,

$$B = \frac{2\pi}{\lambda} \int_{\infty}^R \gamma(I, r) I(r) dr,$$

where  $\gamma$  is small, and depends on the intensity dependent refractive index. Neglecting laser light absorption in the plasma region  $\rho < \rho_c/4$  ( $\rho_c$  is critical density) and assuming that, in this region of plasma density,  $\gamma$  depends on ponderomotive forces only (Hora 1981; Will et al. 1982) the  $B$ -integral is,

$$B = \text{const } 2\pi\lambda I(R_c) \int_{\infty}^{R(\rho_c/4)} \frac{1}{r^3} \frac{1}{kT_e} \frac{\rho(r)}{\rho_c} dr.$$

If  $T_e$  is constant in the plasma region  $\rho_c/10$  to  $\rho_c/4$  and the density distribution is taken according to data obtained with the computer code ‘‘Lutch’’ (Afanasiev et al. 1976) the density distribution can be approximated by,

$$\rho(R) = \rho_c \exp - \left\{ \frac{4\pi}{3} R_c^3 \frac{n_c}{z} \frac{\sum I + (z+1)kT_{ec}}{\xi E_{\text{abs}}} \left[ \left( \frac{R}{R_c} \right)^3 - 1 \right] \right\},$$

where  $R_c$  is the critical surface radius,  $z$  is the effective ion charge,  $\sum I$  is the ionization potential sum,  $E_{\text{abs}}$  is the absorbed energy,  $T_{ec}$  is the electron temperature in the critical region and  $\xi = 0.3$ . Numerical evaluation of the  $B$ -integral with the help of the given formulae gives  $B = 1.4\pi$  for a glass target with a radius,  $R = 225 \mu\text{m}$  and,  $B = 2.4\pi$  for a polystyrene target. As has been seen, the best conditions for self-focusing are in plasma corona at low electron temperature which correspond to the targets of large size and low  $z$ .

Thus, laser radiation self-focusing effectively develops in the plasma corona and may be the reason for the filamentation observed and the compression symmetry destruction.

### 8. Conclusions

The heating and compression experiments, with absorbed energy between 0.3 and 0.5 kJ, using the laser installation ‘Delfin-1’ have shown that high aspect-ratio shells

are preferable for laser fusion experiments. The measured parameters were, volume compression,  $V_0/V = 3.5 \times 10^3$ , mean implosion velocity,  $\bar{c} = 1.6 \times 10^7$  cm/s, final stage velocity  $c = 2.6 \times 10^7$  cm/s and compressed core electron temperature  $T_e \approx 2$  keV. A neutron yield of  $N = 10^6 - 10^7$  in the experiments with  $D_2$  filled shells was observed.

The appearance of plasma corona filamentation correlated with compression symmetry destruction.

## REFERENCES

- AFANASIEV, YU. V., GAMALY, E. G. *et al.* 1982 *Trudy FIAN*, **134**, 52.
- AFANASIEV, YU. V., BASOV, N. G., VASIN, B. L. *et al.* 1979a *JETPH*, **77**, 2539.
- AFANASIEV, YU. V., BASOV, N. G., VOLOSEVICH, P. P. *et al.* 1979b *Preprint FIAN*, N556.
- AFANASIEV, YU. V., GAMALY, E. G. *et al.* 1980 *Preprint FIAN*, N30.
- AFANASIEV, YU. V., VOLOSEVICH, P. P. *et al.* 1976 *JETPH Letts.* **23**, 470.
- ANDRE, M., COURTEILLE, T. C. *et al.* 1978 *XII Europ. Conf. on Laser Interaction with Matter (Moscow)*.
- BASOV, N. G., KOLOGRIVOV, A. A. *et al.* 1977 "Later Interaction and Related Plasma Phenomena", **4**, 479.
- BASOV, N. G., KROKHIN, O. N. & SKLIZKOV, G. V. 1967 *JETPH Letts.* **6**, 683.
- BASOV, N. G., GAMALY, E. G., KROKHIN, O. N. *et al.* 1974 "Laser Interaction and Related Plasma Phenomena", **3B**, 553.
- BASOV, N. G., BYKOVSKY, N. G., DANILOV, A. E. *et al.* 1978 *Trudy FIAN*, **103**, 3.
- BASOV, N. G., VOLOSEVICH, P. P., GAMALY, E. G. *et al.* 1980 *JETPH*, **78**, 420.
- BASOV, N. G., GALICHY, A. A., DANILOV, A. E. *et al.* 1981 "Laser Interaction and Related Plasma Phenomena", **5**, 25.
- BASOV, N. G., DANILOV, A. E., KIRSANOVA, I. V. *et al.* 1982 *Preprint FIAN*, N19.
- BASOV, N. G., KALASHNIKOV, M. P., MIKHAILOV, YU. A. *et al.* 1982 *JETPH Letts.* **8**, 669.
- BUNKENBERG, J. *et al.* 1981 *IEEE J. Quant. Electron.* **QE-17**, 1620.
- DANILOV, A. E., DEMCHENKO, N. N., ROZANOV, V. B. *et al.* 1977 *Kvantovaya Elektronika*, **4**, 1034.
- DANILOV, A. E., MIKHAILOV, YU. A., SKLIZKOV, G. V. & FEDOTOV, S. I. 1978 *Preprint FIAN*, N73.
- HERBST, M. J., STANPER, J. A., WHITLOCK, R. R. *et al.* 1981a *Phys. Rev. Lett.* **46**, 328.
- HERBST, M. J., WHITLOCK, R. R. & YONG, E. C. 1981b *Phys. Rev. Letts.* **47**, 91.
- HORA, H. 1981 "Physics of Laser Driven Plasmas", John Wiley & Sons, New York.
- KATO, Y., YAMANAKA, T., IZAWA, J. & SASAKI, J. 1979 *Annual Progress report on Laser Fusion Program, ILE, Osaka University*.
- KIRILLOV-UGRUMOV, M. V., KOZLOVSKY, K. I., LIAPIDEVSKY, V. K., *et al.* 1981 *PTE*, **2**, 71.
- MOCHIZUKI, T., YABE, T., MIMA, K. *et al.* 1980 *J. Appl. Phys.* **19**, 645.
- NIKOLAEV, F. A., SOROKIN, V. V. *et al.* 1980 *Preprint FIAN*, N157.
- RIPIN, B. H., WHITLOCK, R. R., YONG, F. C. *et al.* 1979 *Phys. Rev. Lett.* **43**, 350.
- SCOBERNE, F. 1978 *Los-Alamos Scientific Lab. Progress Report*, **LA-7328-PR**.
- SEDOV, L. I. 1946 *Prikladnaya Matematika i Mehanyka*, **IX**, 2.
- SPECK, D. R. 1978 *Laser Program Annual Report LLL*, **UCRL-50021-78**, 1
- SPECK, D. R. *et al.* 1979 *Preprint LLL UCRL-82117*.
- VALUEV, A. D., VASIN, B. L., IVANOV, B. YU. *et al.* 1978 *Preprint FIAN*, N239.
- WILL, O. *et al.* 1982 *Rutherford Lab Annual Report*, **PL-82-039**, 18.